

Magnetocrystalline anisotropy of Fe-Si alloys on MgO(001)Y. N. Zhang,¹ J. X. Cao,¹ I. Barsukov,² J. Lindner,² B. Krumme,² H. Wende,² and R. Q. Wu¹¹*Department of Physics and Astronomy, University of California, Irvine, California 92697, USA*²*Fakultät für Physik and Center for Nanointegration (CeNIDE), Universität Duisburg-Essen, Lotharstr. 1, 47048 Duisburg, Germany*

(Received 17 December 2009; revised manuscript received 21 February 2010; published 15 April 2010)

Experimental investigations on magnetic anisotropy energies of epitaxial Fe_{100-x}Si_x thin films on MgO(001) have been extended to low Si concentration. We separated different contributions and found that the strain-induced magnetocrystalline anisotropy term favors an in-plane easy axis for the Fe_{94.5}Si_{5.5} sample, but an out-of-plane easy axis for the Fe₇₅Si₂₅ sample. First principles calculations using the highly precise full potential linearized augmented plane wave method indicated that this results from the sign change in magnetoelastic coupling coefficient in the composition range. Analysis in electronic structures provides clear insights for the understanding of magnetic anisotropy in these films.

DOI: [10.1103/PhysRevB.81.144418](https://doi.org/10.1103/PhysRevB.81.144418)

PACS number(s): 75.50.Bb, 75.30.Gw, 71.20.Be, 76.50.+g

I. INTRODUCTION

Heterojunctions between magnetic materials and semiconductors have attracted special attention due to their potential applications in spintronic devices that require an efficient injection of spin-polarized current into semiconductor for manipulations.¹ The spin polarization rate of currents from conventional magnetic metals is nevertheless small at ambient temperature, and it is hence crucial to find alternative magnetic materials for technological exploitations. Heusler compounds are promising candidates since they show half-metallic ferromagnetic features according to band structure calculations. Their minority-spin band displays a sizable gap around the Fermi level, thus they should produce a 100% spin-polarized current with electrons merely from their metallic majority spin channel. Fe₃Si is a ferromagnetic binary Heusler alloy and was found to have a spin polarization of 43% and a high Curie temperature of 820 K.^{2,3} Bulk Fe-Si is probably among the most widely studied alloy systems in human history, back to year 1889.⁴⁻⁷ Epitaxial Fe-Si thin films on single crystalline substrates such as GaAs and MgO have also been actively explored in recent years, partially motivated by the quest for better magnetic tunneling junctions.⁸⁻¹³ However, understanding of properties of Fe-Si alloy films is still vague in various aspects, in particular regarding the strain-induced magnetic anisotropy that is an important feature for the control of magnetic media. This inspired us to investigate well-ordered epitaxial DO₃-Fe₃Si thin films on MgO(001) using the Ferromagnetic resonance (FMR) technique, aiming at correlating and quantifying individual magnetic anisotropy terms with different growth conditions.^{14,15}

The goal of the present paper is twofold: (i) we extend the experimental work¹⁴ to low Si concentrations by investigating the Fe_{94.5}Si_{5.5} thin film on MgO(001); (ii) we report results of first-principles calculations for magnetic properties of Fe_{100-x}Si_x alloys ($x=6.25-25$) and discuss the physical origin of magnetic anisotropy based on fundamental electronic structures. This lays a foundation for the manipulation of magnetic anisotropy in Fe-Si films, a crucial step for the utilization of these materials in technological applications. In general, the magnetic free energy density of Fe_{100-x}Si_x films takes the form,

$$E = -\vec{M} \cdot \vec{B}_0 + E_{\text{cub}} + E_{\text{shape}} + E_{\text{u}}^{\perp}, \quad (1)$$

where the first Zeeman term is due to the external magnetic field \vec{B}_0 . Using α_i to denote the direction cosines of the magnetization vector with respect to the three axes of cubic lattice, the fourfold cubic magnetocrystalline anisotropy in the second term is given by $E_{\text{cub}} = K_4(\alpha_x^2\alpha_y^2 + \alpha_x^2\alpha_z^2 + \alpha_y^2\alpha_z^2)$. The third term is the shape anisotropy from magnetic dipole interactions. For a homogeneously magnetized thin film it can be written as $E_{\text{shape}} = \frac{\mu_0}{2} \cdot M^2 \alpha_z^2$. Finally, the strain-induced uniaxial magnetocrystalline anisotropy is given by $E_{\text{u}}^{\perp} = -K_{2\perp} \cdot \alpha_z^2$. Due to the same angular variation of E_{u}^{\perp} and E_{shape} , accurate measurement of magnetization is needed to separate them.

While E_{shape} always favors an in-plane easy axis, the magnitude and sign of E_{u}^{\perp} strongly depend on lattice strain, surface and interface conditions, and compositions of thin films. It has been an intriguing research subject in recent years to find thin film materials with sufficiently large positive $K_{2\perp}$ for the realization of perpendicular magnetization. For the epitaxial DO₃-Fe₃Si thin films on MgO(001), we found that the E_{u}^{\perp} term tends to align magnetization out-of-plane.¹⁴ It is interesting that Fe_{94.5}Si_{5.5} intrinsically prefers an in-plane alignment, in contrast to the result for Fe₇₅Si₂₅. Our density functional calculations reproduced experimental data for both concentrations and furthermore we explained the mechanism through analyses in band structures.

II. EXPERIMENTAL DETAILS AND RESULTS

The epitaxial 8 nm thick Fe₇₅Si₂₅ film and the 11 nm thick Fe_{94.5}Si_{5.5} film were grown on MgO(001) in a molecular beam epitaxy (MBE) system with a base pressure of about 1×10^{-10} mbar. The MgO(001) substrate was first cleaned by isopropanol in an ultrasonic bath and afterward transferred into the MBE chamber. The substrate was annealed at 1200 K for 30 min. The films were grown by co-evaporation of Fe and Si at a substrate temperature of $T=485$ K and a growth rate of about 1 nm/min, which was monitored by a calibrated quartz microbalance. In order to avoid any oxidation, the samples were capped with 5 nm of chromium. To verify that the capping layer has no influence on the mag-

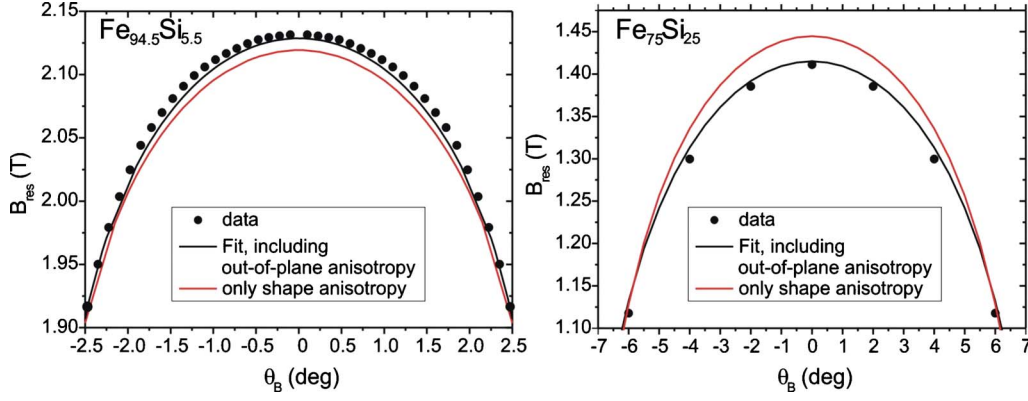


FIG. 1. (Color online) Angular dependence of the FMR resonance field as function of the out-of-plane angle of the external magnetic field obtained at ambient temperature and a microwave frequency of 9.9 GHz for the $\text{Fe}_{94.5}\text{Si}_{5.5}$ (left panel) and the $\text{Fe}_{75}\text{Si}_{25}$ (right panel) samples. The maximum of the resonance field at $\theta_B=0$ indicates that both films have an effective in-plane anisotropy. The black fitting curves are used to extract the anisotropy values, whereas the red (light gray) curves show only the shape anisotropy.

netic properties, uncapped films were also produced for comparison. Within the accuracy of the measurement there is no difference between these two films. The structure and stoichiometry of samples were verified using x-ray diffraction (XRD) and energy dispersive x-ray analysis (EDX). While XRD and Mössbauer spectroscopy confirmed the DO_3 structure for the $\text{Fe}_{75}\text{Si}_{25}$ system (see also Ref. 14) and an A2 structure for the $\text{Fe}_{94.5}\text{Si}_{5.5}$ film, from EDX we found that the chemical composition was accurate within an error of 0.5%.

The angular dependent FMR experiments were performed at ambient temperature at a fixed microwave frequency of 9.9 GHz. The magnetization of the film was determined by superconducting quantum interference device (SQUID) magnetometry. To obtain the best accuracy for film volumes, the lateral dimensions were measured by optical microscopy, while thicknesses were checked by atomic force microscopy (AFM). The angular dependence of the FMR resonance field can be derived from the free energy density with the approach introduced by Smit and Berljers.¹⁶ For details of the procedure to obtain the resonance field as function of the in-plane (azimuthal) angle and the out-of-plane (polar) angle of the external magnetic field we refer the reader to Ref. 14). The results are

$$\left(\frac{\omega}{\gamma}\right)^2 = \left(B_{\text{res},\parallel} \cos \Delta\varphi - \mu_0 M_{\text{eff}} + \frac{K_4}{2M} [3 + \cos 4\varphi_{\text{eq}}] \right) \cdot \left(B_{\text{res},\parallel} \cos \Delta\varphi + \frac{2K_4}{M} \cos 4\varphi_{\text{eq}} \right) \quad (2)$$

for the in-plane angular dependence and

$$\left(\frac{\omega}{\gamma}\right)^2 = \left(B_{\text{res},\perp} \cos \Delta\theta + \left[\mu_0 M_{\text{eff}} + \frac{K_4}{2M} \right] \cos 2\theta_{\text{eq}} + \frac{3K_4}{2M} \cos 4\theta_{\text{eq}} \right) \cdot \left(B_{\text{res},\perp} \cos \Delta\theta + \left[\mu_0 M_{\text{eff}} + \frac{K_4}{M} \right] \cos^2 \theta_{\text{eq}} + \frac{3K_4}{M} \cos^4 \theta_{\text{eq}} - \frac{2K_4}{M} \right) \quad (3)$$

for the out-of-plane angular dependence for which the external magnetic field is varied within the plane defined by the $[001]$ -direction (film normal) and the (110) in-plane direction. The quantities $\Delta\varphi = \varphi_{\text{eq}} - \varphi_B$ and $\Delta\theta = \theta_{\text{eq}} - \theta_B$ are the difference between the angle of the external magnetic field (φ_B and θ_B for azimuthal and polar dependence, respectively) and the equilibrium angle of the magnetization (φ_{eq} and θ_{eq}). Note that the magnetization needs not necessarily follow the external magnetic field direction due to the presence of magnetic anisotropy. $\mu_0 M_{\text{eff}} = \frac{2K_{2\perp}}{M} - \mu_0 M$ is the effective out-of-plane anisotropy field, $\omega = 2\pi f$ the microwave frequency and $\gamma = g \frac{\mu_B}{\hbar}$ the spectroscopic splitting factor. The two equations above yield complete angular dependencies of the in-plane resonance field $B_{\text{res},\parallel}$ as function of the azimuthal angle φ_B of the external field as well as the out-of-plane dependence of the resonance field $B_{\text{res},\perp}$ as function of the polar angle θ_B of the external field. The equilibrium angles of the magnetization are determined by minimizing the free energy. The two equations are used to extract the anisotropy values by fitting them to the measured angular dependencies. In addition to angular dependent FMR studies, frequency dependent measurements using microwave frequencies of 9.8, 23.8, and 33.5 GHz were carried out. By means of those the g factor was obtained in accordance with Eq. (2) and further utilized for exact fitting of the angular dependent data.¹⁷

Figure 1 shows the out-of-plane angular dependence for the $\text{Fe}_{94.5}\text{Si}_{5.5}$ (left panel) and $\text{Fe}_{75}\text{Si}_{25}$ (right panel) film. The data for the $\text{Fe}_{75}\text{Si}_{25}$ sample has been reproduced from Ref. 14 and the attention here should be directed to the behavior to external magnetic field angles around the out-of-plane direction, $\theta_B=0$. Two fitting curves are shown: one includes all magnetic anisotropies as discussed in Ref. 14 (black curve) and another one (red/light gray curve) includes only the shape anisotropy, using $\mu_0 M = 1.842(45)$ T for the $\text{Fe}_{94.5}\text{Si}_{5.5}$ sample and $\mu_0 M = 1.105(30)$ T for the $\text{Fe}_{75}\text{Si}_{25}$ sample obtained from separate SQUID measurements. The difference between the two curves thus stems from to the intrinsic uniaxial magnetocrystalline anisotropy E_u^\perp . Strikingly, while $K_{2\perp}$ is positive (11.0 ± 4.0 kJ/m³, favoring an out-of-plane easy axis) for the $\text{Fe}_{75}\text{Si}_{25}$ sample in the right panel, it becomes negative (-5.85 ± 2.0 kJ/m³, favoring an in-plane

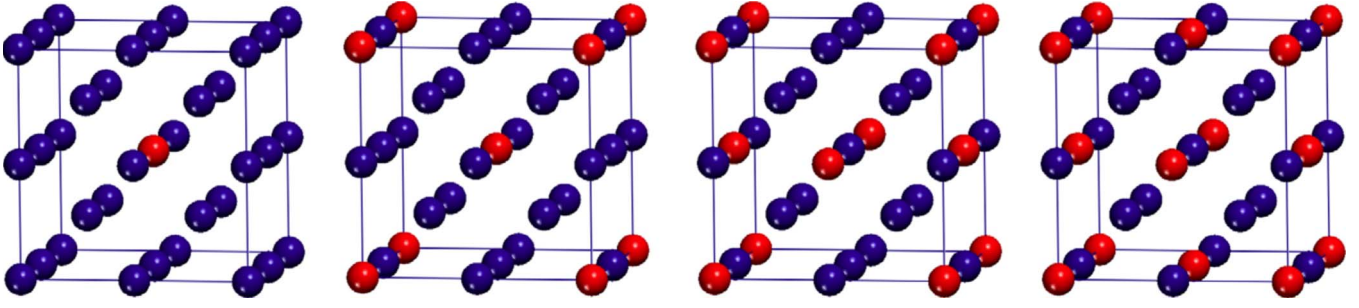


FIG. 2. (Color online) Atomic configurations for the cubic structures of $\text{Fe}_{100-x}\text{Si}_x$ alloy with $x=6.25, 12.5, 18.75,$ and 25 . Blue (dark) and orange (light) spheres represent Fe and Si atoms, respectively.

easy axis) for the $\text{Fe}_{94.5}\text{Si}_{5.5}$ sample in the left panel. One should note that nevertheless both systems are magnetized in-plane due to the much larger E_{shape} .

III. COMPUTATIONAL DETAILS AND RESULTS

To attain clear physical insights for the experimental data, we also performed first-principles calculations for the magnetic anisotropy of $\text{Fe}_{100-x}\text{Si}_x$ alloys ($x=6.25 \sim 25$). The all-electron full potential linearized augmented plane wave (FLAPW) method¹⁸ was used to solve the density functional Kohn-Sham equations, along with the generalized gradient approximation for the description of exchange-correlation interaction.¹⁹ No shape approximation was assumed in charge, potential, and wave function expansions. The core electrons were treated fully relativistically, while the spin-orbit coupling term was invoked second variationally for the valence states.²⁰ Energy cutoffs of 225 and 16 Ry were chosen for the charge-potential and basis expansions in the interstitial region. Spherical harmonics with a maximum angular momentum of $l_{\text{max}}=8$ were used in the muffin-tin region ($r_{\text{Fe}}=2.30$ a.u., $r_{\text{Si}}=2.10$ a.u.). We adopted 550 k points to sample the irreducible Brillouin zone (BZ), and the self-consistency was assumed when the root-mean-square differences between the input and output charges and spin densities were less than 1.0×10^{-4} e/(a.u.)³.

For the $\text{Fe}_{100-x}\text{Si}_x$ alloy grown on the MgO(001) surface, two factors may contribute to the intrinsic magnetic anisotropy: tetragonal strain in the lattice and the presence of surface and interface. Since experimental data were measured from thick films (8 nm for $\text{Fe}_{75}\text{Si}_{25}$ and 11 nm for $\text{Fe}_{94.5}\text{Si}_{5.5}$), the surface/interface effects can be ignored to good approximation. We hence focus on magnetic anisotropy induced by tetragonal strain in the films due to lattice mismatch. Supercell models with 16 atoms as sketched in Fig. 2 were used in our calculations for $\text{Fe}_{100-x}\text{Si}_x$ ($x=6.25 \sim 25$) alloys. According to the phase diagram, Fe-Si alloys tend to adopt the DO_3 structure when Si concentration is between 12.5% and 30%.²¹ For high Si concentrations, both A2-like and DO_3 -like atomic arrangements were investigated and we found that DO_3 -type structures are indeed more preferred. The lattice sizes and atomic positions of these structures were optimized according to the energy minimization procedures guided by atomic forces with a criterion that atomic force on each atom is less than 0.01 eV/Å.

The torque approach adopted here has been proved to be an effective method for the reliable determination of magnetic anisotropy energy.²⁰ To investigate the effect of lattice distortion on $K_{2\perp}$, we applied a tetragonal strain $\varepsilon_z \equiv \varepsilon$ along the z axis within a range of -2% to $+2\%$ in the constant-volume mode (i.e., $\varepsilon_x = \varepsilon_y = -\varepsilon/2$). The calculated strain dependences of $K_{2\perp}$ for DO_3 - $\text{Fe}_{75}\text{Si}_{25}$ and A2- $\text{Fe}_{93.75}\text{Si}_{6.25}$ are illustrated in Fig. 3. The smoothness of data points indicates the high precision of the present calculations, even though the amplitude of $K_{2\perp}$ is typically very small.

Obviously, the slope of the $K_{2\perp} \sim \varepsilon$ line ($dK_{2\perp}/d\varepsilon$) is negative for the DO_3 - $\text{Fe}_{75}\text{Si}_{25}$, implying that a compressive strain along the interface normal induces positive $K_{2\perp}$. As already reported in Ref. 14, x-ray diffraction studies revealed that the vertical lattice size of the $\text{Fe}_{75}\text{Si}_{25}$ film is $a_{\perp} = 0.563$ nm, 0.3% smaller than the cubic $\text{Fe}_{75}\text{Si}_{25}$ bulk lattice constant $a_{\text{bulk}}(\text{Fe}_{75}\text{Si}_{25}) = 0.565$ nm. Considering the vertical strain of -0.3% , the calculated $K_{2\perp}$ is $+12.8$ kJ/m³. This is in good agreement with experimental measurement (11.0 ± 4.0 kJ/m³, see the filled up-triangle in the inset of Fig. 3). In the same plot, interestingly, one observes that $dK_{2\perp}/d\varepsilon$ for $\text{Fe}_{93.75}\text{Si}_{6.25}$ is positive, indicating an in-plane contribution under a compressive strain along the z axis. Experimentally, the vertical lattice constant for the $\text{Fe}_{94.5}\text{Si}_{5.5}$ thin film was found to be $a_{\perp} = 0.571$ nm. As no bulk reference sample was available, one may compare this to the bulk

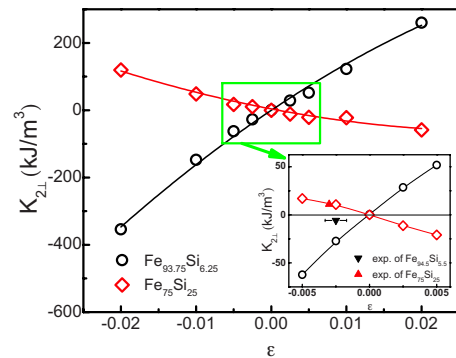


FIG. 3. (Color online) The uniaxial anisotropy energy $K_{2\perp}$ of $\text{Fe}_{93.75}\text{Si}_{6.25}$ (open circles) and $\text{Fe}_{75}\text{Si}_{25}$ (open diamonds) as a function of strains along the z axis. The inset is the enlarged $K_{2\perp} \sim \varepsilon$ curve within the strain range of -0.5% to $+0.5\%$. The experimental data for $\text{Fe}_{94.5}\text{Si}_{5.5}$ (down-triangle) and $\text{Fe}_{75}\text{Si}_{25}$ (up-triangle) are also shown for comparison. The horizontal bar shows the possible range of strain for $\text{Fe}_{94.5}\text{Si}_{5.5}$, -0.17% to -0.33% .

TABLE I. Calculated spin magnetic moments, slope of the $K_{2\perp} \sim \varepsilon$ curve, $K_{2\perp}$ at $\varepsilon = -0.3\%$, and the cubic anisotropy constant K_4 of $\text{Fe}_{100-x}\text{Si}_x$ alloys.

$\text{Fe}_{100-x}\text{Si}_x$ $x=$	μ_{tot} ($\mu_{\text{B}}/\text{cell}$)	$\mu_{\text{Fe(C)}}$ ($\mu_{\text{B}}/\text{atom}$)	$dK_{2\perp}/d\varepsilon$ (kJ/m^3)	$K_{2\perp}$ at $\varepsilon = -0.3\%$ (kJ/m^3)	K_4 (kJ/m^3)	λ (10^{-6})
6.25	31.65	2.08	13971.6	-41.9	19.4	53
12.5	27.06	1.74	7907.2	-23.7	15.6	33
18.75	24.31	1.62	-3999.8	12.0	-13.1	-22
25	20.06	1.33	-4271.3	12.8	4.6	-11

Fe value of $a_{\text{bulk}}(\text{Fe}) = 0.5732$ nm. This means that the $\text{Fe}_{94.5}\text{Si}_{5.5}$ film is under a compression of about 0.33%. Reference 22 reported that the bulk lattice constant of the bulk $\text{Fe}_{95}\text{Si}_5$ is about 0.572 nm, resulting in a compression of about 0.17%. We assume that the actual lattice compression in the $\text{Fe}_{94.5}\text{Si}_{5.5}$ film lies in this range ($\varepsilon = -0.17$ – -0.33% , as shown by the horizontal bar in the inset of Fig. 3) and the calculated $K_{2\perp}$ of $\text{Fe}_{93.75}\text{Si}_{6.25}$ is expected to be between -24 to -46 kJ/m^3 . The agreement between theory and experiment should be still reasonable considering the uncertainty regarding the real value of ε in experimental samples.

To provide a general trend of the strain-induced uniaxial magnetic anisotropy, we give $dK_{2\perp}/d\varepsilon$ of $\text{Fe}_{100-x}\text{Si}_x$ alloys at different x in Table I, together with the values of $K_{2\perp}$ at a fixed compressive strain, -0.3% . Obviously, $K_{2\perp}$ changes its sign between $x = 12.5$ – 18.75% , as observed in our experiments. Similar trend was also found from $\text{Fe}_{100-x}\text{Ge}_x$ alloys,^{23,24} for which the magnetoelastic coupling constant changes its sign at $x = 14\%$. One may find that the magnetic moments of $\text{Fe}_{100-x}\text{Si}_x$ alloys decrease linearly with increasing Si content. Specially, the magnetic moments of Fe(C) atoms, which have tetrahedral point symmetry with four Fe and four Si nearest neighbors in the DO_3 structure, become significantly smaller than that in the bulk bcc Fe. The calculated magnetic moment for Fe(C) in $\text{Fe}_{75}\text{Si}_{25}$, $1.33\mu_{\text{B}}$, also agrees excellently with the experimental data, $1.35\mu_{\text{B}}$.²

Furthermore, we also calculated the cubic bulk magnetic anisotropy energies for $\text{Fe}_{100-x}\text{Si}_x$. The cubic magnetic anisotropy coefficient K_4 can be determined experimentally by using the magnetization curves in $[100]$, and $[110]$ directions.^{25,26} In the *ab initio* studies, K_4 can be obtained by evaluating the angle derivative of total energy at the polar angle $\theta = 22.5^\circ$ away from the z axis (see the details in Ref. 21). The cubic magnetic anisotropy energy is only about 1 $\mu\text{eV}/\text{atom}$ due to the high symmetry. The determination of such small energies through density functional calculations is still very challenging. In the present calculations, 67200 k -points were used in the full BZ to obtain converged results of K_4 . As listed in Table I, it is striking to note that K_4 also linearly decreases with x , in line with experimental observations.¹⁰ Quantitatively, the calculated K_4 for $DO_3\text{-Fe}_{75}\text{Si}_{25}$ (4.6 kJ/m^3) is very close to the result reported in Ref. 14 (4.0 kJ/m^3). We thus believe that the calculated K_4 values for other systems are also reliable and further experiment work will be performed to verify them.

IV. DISCUSSIONS

It is obvious that first principle calculations correctly produced both the uniaxial and cubic terms of magnetocrystal-

line anisotropy energies of $\text{Fe}_{100-x}\text{Si}_x$ alloys under tetragonal distortions. It is thus possible and desirable to unravel the driving factor through analysis on fundamental properties such as band structures and wave functions. To this end, we first resolve the contributions to the $K_{2\perp}$ from different regions in the BZ, starting from examining the $K_{2\perp} \sim k_z$ dependence (obtained by integrating contributions in each k_x - k_y plane). For $\text{Fe}_{75}\text{Si}_{25}$, the $K_{2\perp}(k_z)$ curve in Fig. 4 shows a balance between positive contributions in the region $0 < k_z < 0.188$ and negative contributions in the region $0.188 < k_z < 0.29$ for the cubic DO_3 lattice (black squares). A negative vertical strain (blue triangles) enhances the positive contributions but depresses the negative contributions and thus produces a positive $K_{2\perp}$, as was presented in Fig. 3. We further “zoom in” toward the most active region, and show distributions of $K_{2\perp}$ in the k_x - k_y planes at $k_z = 0.188$ a.u. (or slightly changed under distortions) in the insets. This procedure allows us to see exactly which part of BZ and which states are responsible to the strain dependence of $K_{2\perp}$. Here, the red and blue dots represent positive and negative contributions to $K_{2\perp}$, and their sizes show magnitudes. For $\text{Fe}_{75}\text{Si}_{25}$, the most eye-catching region is red region around $1/5(\Gamma\text{-M})$, where both the area and magnitude sensitively

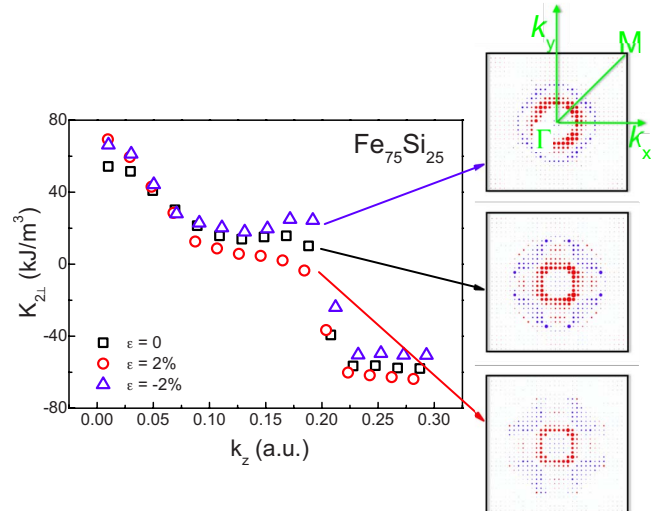


FIG. 4. (Color online) The distribution of $K_{2\perp}$ along the k_z axis in the 3D BZ of the $DO_3\text{-Fe}_{75}\text{Si}_{25}$. Circles, squares, and triangles are for cases with $\varepsilon = 2\%$, 0% , and -2% , respectively. The insets display the distributions of $K_{2\perp}$ in the k_x - k_y planes at $k_z = 0.188$ a.u. Red (light gray) and blue (dark-gray) spots are for positive and negative contributions to $K_{2\perp}$ from different (k_x, k_y) points and their size scales with the magnitude of $K_{2\perp}$.

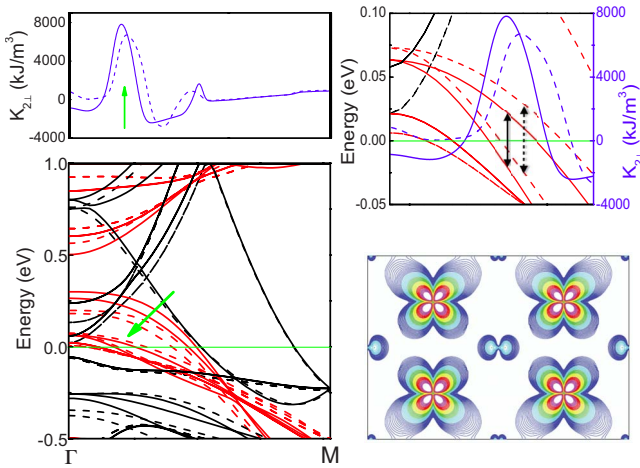


FIG. 5. (Color online) The band structure along the diagonal direction of the two-dimensional Brillouin zone at a fixed $k_z \approx 0.188$ a.u. for the cubic (solid lines) and distorted ($\varepsilon = -2\%$, dashed lines) DO_3 - $Fe_{75}Ga_{25}$, respectively. The black lines are for the majority spin, and the red (light gray) ones are for the minority spin. The blue (dark-gray) lines in the upper-left and upper-right panels are for the distribution of $K_{2\perp}$ along the k -points. Contours in the lower-right panel display the wave function features of the key states discussed in the text.

change with vertical strains. For instance, this region expands for $\varepsilon = 0 \rightarrow -2\%$, but shrinks as $\varepsilon = 0 \rightarrow +2\%$.

As a further step, we calculated the band structure and the k -dependence of $K_{2\perp}(k)$ along the $(\Gamma$ -M) direction in the BZ at $k_z = 0.188$ a.u., for two different lattice strains. Again, it is obvious in Fig. 5 that the major contributions to $K_{2\perp}$ are from the vicinity near $1/5(\Gamma$ -M). The availability of the detailed band structures and matrix elements allows us to ultimately trace down to key electronic states. In this region, we found a pair of t_{2g} (or $d_{xz,yz}$) states across the Fermi level in the minority spin channel, with their features displayed in the lower-right panel of Fig. 5. They are localized at the Fe(C) atom and are close in energy and, moreover, they have large spin-orbit coupling interaction. Since they have the same magnetic quantum number ($m = \pm 1$) and are in the same spin channel, they produce large positive contribution to $K_{2\perp}$ through $\langle xz | L_z | yz \rangle$, according to the perturbation theory.²⁷ Lattice compression along the z axis causes the occupied and unoccupied $d_{xz,yz}$ bands to move up in energy and the region where they stay separated by the Fermi level expands in the BZ. As a result, a positive $K_{2\perp}$ is produced, as found in both theory and experiment.

Analyses on contributions to $K_{2\perp}$ were also done for the $Fe_{93.75}Si_{6.25}$ case. As shown in Fig. 6, the most active region in $K_{2\perp}(k_z)$ is near the center of the BZ, namely, at $k_z = 0$. Negative contributions are further enhanced by negative strain, as demonstrated by the motion of the $K_{2\perp}(k_z)$ line under tetragonal distortion. The projections of $K_{2\perp}$ in the k_x - k_y plane ($k_z = 0$) in the insets of Fig. 6 indicate that most pronounced changes of $K_{2\perp}$ actually happens near the $\bar{\Gamma}$ point. A red region appears at the center of the BZ for $Fe_{93.75}Si_{6.25}$ under positive tetragonal strain but the negative contributions dominate for cases with zero or negative strains. Results of band structures with the fixed k_z (not

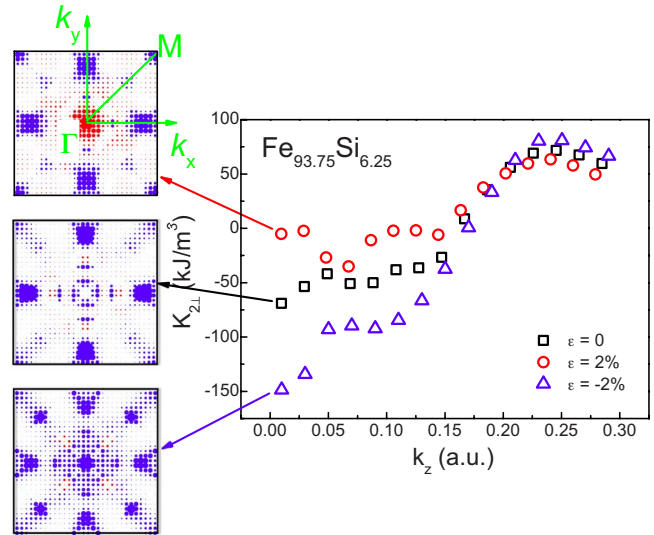


FIG. 6. (Color online) The distribution of $K_{2\perp}$ along the k_z axis in the three-dimensional (3D) BZ of the $Fe_{93.75}Si_{6.25}$ alloy. The insets are the distributions of $K_{2\perp}$ in the k_x - k_y planes when $k_z = 0$. Red (light gray) and blue (dark-gray) spots are for positive and negative contributions to $K_{2\perp}$ from different (k_x, k_y) points and their size scales with the magnitude of $K_{2\perp}$.

shown here) reveal that the response of $K_{2\perp}$ to lattice strain stems from the change in occupation of d_{xy} state. As was also discussed before for the bulk Fe,²⁸ the relative energy shifts and changes of occupations of d states of the Fe(C) atom under a negative ε enhances the in-plane contributions but weakens the perpendicular contributions to $K_{2\perp}$.

V. CONCLUSIONS

In summary, the electronic and magnetic anisotropic properties of $Fe_{100-x}Si_x$ alloys in A2 or DO_3 structures have been studied through experimental measurements and first-principles calculations. We found that the magnetization direction of $Fe_{100-x}Si_x$ films grown on MgO(001) under compressive vertical strain change from in-plane to out-of-plane at silicon concentration between 12% and 18.75%. Theory and experiment achieved satisfactory agreement and thus validate the further electronic structure analysis. Through decomposition procedures in the Brillouin zone, we traced down key electronic states, such as the Fe(C)- $d_{xz,yz}$ states for $Fe_{75}Si_{25}$, for the unusual magnetoelastic coupling behaviors of these alloys. These studies provide insights for the use of $Fe_{100-x}Si_x$ alloys as spintronic materials. Furthermore, the enhanced magnetoelastic coupling is also essential for the understanding of magnetostriction, another significant subject that is currently under active interdisciplinary investigations.^{29,30}

ACKNOWLEDGMENTS

The experimental work was supported by the Deutsche Forschungsgemeinschaft (DFG, Sfb 491); theoretical work was supported by the ONR (Grant No. N00014-08-1-0143)

and by the NSF (Grant No. DMR-0706503). One of us (J.L.) also thanks the Alexander von Humboldt Foundation for sup-

port through the Feodor Lynen program. Calculations were performed on the DOD parallel computers.

-
- ¹G. A. Prinz, *Science* **282**, 1660 (1998).
- ²V. A. Niculescu, T. J. Burch, and J. I. Budnick, *J. Magn. Magn. Mater.* **39**, 223 (1983).
- ³Y. Nakamura, *Alloys and Compounds of d-Elements with Main Group Elements*, Landolt-Börnstein New Series, Group III, Vol. 19, Part C (Springer, Berlin, 1988), p. 26.
- ⁴R. A. Hadfield, *J. Iron Steel Inst. II* (London) **1889**, 222.
- ⁵W. F. Barret, W. Brown, and R. A. J. Hadfield, *Sci. Trans. Roy. Dublin Soc.* **7**, 67 (1900); *J. Inst. Electr. Eng.* **31**, 674 (1902); H. J. Williams, *Phys. Rev.* **52**, 747 (1937); L. P. Tarasov, *ibid.* **56**, 1231 (1939); S. Arajs, H. Chessin, and D. S. Miller, *J. Appl. Phys.* **32**, 857 (1961); V. D. Solovei, and Yu. N. Dragoshanskii, *Phys. Met. Metallogr.* **103**, 33 (2007).
- ⁶L. Püst and Z. Frait, *Phys. Lett. A* **86**, 48 (1981).
- ⁷T. Sugano, M. Kinoshita, I. Shirovani, and K. Ohno, *Solid State Commun.* **45**, 99 (1983).
- ⁸J. Kudrnovský, N. E. Christensen, and O. K. Andersen, *Phys. Rev. B* **43**, 5924 (1991).
- ⁹E. G. Moroni, W. Wolf, J. Hafner, and R. Podloucky, *Phys. Rev. B* **59**, 12860 (1999).
- ¹⁰J. E. Mattson, S. Kumar, E. E. Fullerton, S. R. Lee, C. H. Sowers, M. Grimsditch, S. D. Bader, and F. T. Parker, *Phys. Rev. Lett.* **71**, 185 (1993).
- ¹¹J. Herfort, H.-P. Schönherr, and K. H. Ploog, *Appl. Phys. Lett.* **83**, 3912 (2003); J. Herfort, H.-P. Schönherr, K.-J. Friedland, and K. H. Ploog, *J. Vac. Sci. Technol. B* **22**, 2073 (2004); J. Herfort, H.-P. Schönherr, A. Kawaharazuka, M. Ramsteiner, and K. H. Ploog, *J. Cryst. Growth* **278**, 666 (2005); B. Jenichen, V. M. Kaganer, W. Braun, J. Herfort, R. Shayduk, and K. H. Ploog, *Thin Solid Films* **515**, 5611 (2007).
- ¹²A. Kawaharazuka, M. Ramsteiner, J. Herfort, H.-P. Schönherr, H. Kostial, and K. H. Ploog, *Appl. Phys. Lett.* **85**, 3492 (2004).
- ¹³K. Lenz, E. Kosubek, K. Baberschke, J. Herfort, H.-P. Schönherr, and K. H. Ploog, *Phys. Status Solidi C* **3**, 122 (2006).
- ¹⁴Kh. Zakeri, I. Barsukov, N. K. Utochkina, F. M. Römer, J. Lindner, R. Mechenstock, U. vonHörsten, H. Wende, S. S. Kalarickal, K. Lenz, and Z. Frait, *Phys. Rev. B* **76**, 214421 (2007).
- ¹⁵B. Krumme, C. Weis, H. C. Herper, F. Stromberg, C. Antoniak, A. Warland, E. Schuster, P. Srivastava, M. Walterfang, K. Fauth, J. Minár, H. Ebert, P. Entel, W. Keune, and H. Wende, *Phys. Rev. B* **80**, 144403 (2009).
- ¹⁶J. Smit and H. G. Beljers, *Philips Res. Rep.* **10**, 113 (1955).
- ¹⁷B. Heinrich and J. F. Cochran, *Adv. Phys.* **42**, 523 (1993).
- ¹⁸E. Wimmer, H. Krakauer, M. Weinert, and A. J. Freeman, *Phys. Rev. B* **24**, 864 (1981); M. Weinert, E. Wimmer, and A. J. Freeman, *ibid.* **26**, 4571 (1982).
- ¹⁹J. P. Perdew, *Phys. Rev. B* **33**, 8822 (1986); J. P. Perdew, K. Burke, and M. Ernzelhof, *Phys. Rev. Lett.* **77**, 3865 (1996).
- ²⁰R. Q. Wu and A. J. Freeman, *J. Magn. Magn. Mater.* **200**, 498 (1999).
- ²¹T. B. Massalski, *Binary Alloy Phase Diagrams* (American Society for Metals, Ohio, 1986).
- ²²A. Machová, V. Paidar, and F. Kroupa, *Phys. Status Solidi A* **42**, 713 (1977).
- ²³J. X. Cao, Y. N. Zhang, W. J. Ouyang, and R. Q. Wu, *Phys. Rev. B* **80**, 104414 (2009).
- ²⁴D. Wu, Q. Xing, R. W. McCallum, and T. A. Lograsso, *J. Appl. Phys.* **103**, 07B307 (2008).
- ²⁵S. Rafique, J. R. Cullen, M. Wuttig, and J. Cui, *J. Appl. Phys.* **95**, 6939 (2004).
- ²⁶A. E. Clark, M. Wun-Fogle, J. B. Restorff, K. W. Dennis, T. A. Lograsso, and R. W. McCallum, *J. Appl. Phys.* **97**, 10M316 (2005).
- ²⁷D. S. Wang, R. Q. Wu, and A. J. Freeman, *Phys. Rev. B* **47**, 14932 (1993).
- ²⁸S. C. Hong, W. S. Yun, and R. Q. Wu, *Phys. Rev. B* **79**, 054419 (2009).
- ²⁹A. E. Clark, J. B. Restorff, M. Wun-Fogle, T. A. Lograsso, and D. L. Schlagel, *IEEE Trans. Magn.* **36**, 3238 (2000).
- ³⁰E. M. Summers, T. A. Lograsso, and M. Wun-Fogle, *J. Mater. Sci.* **42**, 9582 (2007).